# JOURNAL PRE-PROOF

This is an early version of the article, published prior to copyediting, typesetting, and editorial correction. The manuscript has been accepted for publication and is now available online to ensure early dissemination, author visibility, and citation tracking prior to the formal issue publication.

It has not undergone final language verification, formatting, or technical editing by the journal's editorial team. Content is subject to change in the final Version of Record.

To differentiate this version, it is marked as "PRE-PROOF PUBLICATION" and should be cited with the provided DOI. A visible watermark on each page indicates its preliminary status.

The final version will appear in a regular issue of *Engineering Transactions*, with final metadata, layout, and pagination.
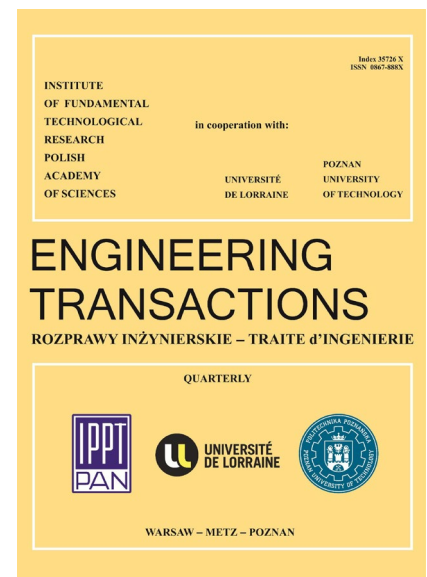
Please cite this article as:

Sobierańska A., Wcisło B., Numerical modeling of aluminum alloy AW5083 using large strain thermo-elasto-plasticity, *Engineering Transactions*, 2025, https://doi.org/10.24423/engtrans.2025.3639

Numerical modeling of aluminum alloy AW5083 using large strain thermo-elasto-plasticity

Agnieszka SOBIERAŃSKA[1], Balbina WCISŁO[1]*

[1]*Chair of Computational Engineering, Cracow University of Technology, Poland*
*Corresponding author e-mail: balbina.wcislo@pk.edu.pl

Abstract

This paper deals with the constitutive modeling and finite element simulations of advanced models related to large strain thermo-elasto-plastic behavior of aluminum alloy AW5083, which can reproduce the material response at different temperatures from room temperature up to 500 degrees Celsius. Significant focus is placed on the internal sources of cooling and heating resulting from thermo-elastic and thermo-plastic couplings, respectively, and the influence of elevated temperature on couplings. The formulation of the constitutive description is based on the thermodynamic approach. Two models are presented and tested: including temperature-dependent and temperature-independent plastic free energy function. Numerical tests of the developed models are carried out for a uniaxial tension test. For the sake of comparison with experimental results, a dogbone specimen examined in a tensile machine is analyzed.

Keywords

aluminum alloy AW5083, thermo-elasto-plasticity, temperature dependent parameters, large strains, finite element method

1 Introduction

This paper presents a constitutive modeling and numerical investigation of aluminum alloy AW5083 using a large strain thermo-elasto-plastic model that incorporates internal heat sources and temperature-dependent material parameters.

Various large strain thermo-elasto-plasticity models can be found in the literature. This work is focused on thermodynamically consistent models presented e.g. in [1] or [2], derived basing on the first and second laws of thermodynamics. Such an approach leads to a formulation which involves internal (often called structural) sources of cooling or heating in the analyzed material. In particular, thermo-elastic coupling related to the Gough-Joule effect, typically associated with entropic materials such as polymers [3], manifests itself for aluminum in cooling for tensioned samples in the elastic regime, whereas the thermomechanical coupling for plasticity results in a temperature increase due to plastic dissipation. The crucial quantity in these formulations is the Helmholtz free energy which can include a reversible part (related to elasticity and thermal expansion), a plastic part and a purely thermal part [2].

Constitutive modeling of an aluminum alloy undergoing large strains at elevated temperatures requires an introduction of temperature-dependent material parameters. Such models are included in some papers, e.g. in [4] presenting a small strain constitutive model for case hardening steel, or in [5] related to thermo-elasto-plasticity of metals with material properties being linear functions of temperature. In this work the

material model based on [2] is enhanced with the dependencies of material properties on temperature, basing on paper [6] and Eurocode [7]. Moreover, the study focuses on two distinct models of the plastic part of the free energy: one that accounts for temperature-dependent material parameters in the free energy formulation and another that assumes temperature-independent hardening in plasticity.

The goal of this research is to develop and test a comprehensive constitutive framework capable of accurately predicting the response of aluminum alloy AW5083 under mechanical loads at different temperatures, ranging from 20°C up to 500°C. The research is a continuation of the work presented in [8], which was restricted to room temperature. The following assumptions are taken into account in the research. The material is initially isotropic, also regarding hardening for plasticity, and associative plastic flow is applied. The model reproduces quasi-static case thus it does not include viscous effects in elasticity nor in plasticity and the inertial term in the balance of linear momentum is dropped. The thermomechanical coupling incorporates thermal expansion, temperature-dependent parameters, internal heat sources and the influence of geometry change on the heat flow in the material, i.e. it takes into account the Fourier law in the deformed configuration.

This advanced and strongly non-linear model is implemented and tested utilizing symbolic-numerical packages *AceGen/AceFEM* of *Wolfram Mathematica* [9]. Simulations are performed for a uniaxial tension test and for a dogbone specimen typically used in experimental conditions [10]. By comparing the selected models, the paper aims to show the influence of temperature-hardening coupling on the mechanical and thermal behavior of the material. The key phenomena of thermo-elastic cooling and heat generation due to plastic dissipation are analyzed in detail. Through numerical simulations of the dogbone specimen, the study explores the effects of temperature-dependent parameters, mesh refinement sensitivity, and thermal boundary conditions on the specimen's response. The results highlight the significance of thermo-plastic coupling in the plastic part of the free energy in reducing self-heating and softening effects, particularly in the temperature range of 200-300°C. The paper also addresses different forms of localization.

The research presented in the paper can be applied for advanced numerical simulations of structures and elements made of aluminum alloy AW5083, which is widely used in shipbuilding, railroad cars, pressure vessels and many other fields, under various mechanical and/or thermal loading. The development of a formulation valid at elevated temperatures enables simulations under fire conditions.

The paper is laid out as follows. Section 2 presents the formulation of the thermo-elasto-plastic material model based on the laws of thermodynamics. Section 3 contains functional dependencies of material parameters, both the mechanical and thermal ones, with respect to temperature. The core part of the paper is Section 4 including the description and results of numerical simulations, whereas conclusion and final remarks are provided in Section 5.

The notation used in the paper is as follows: round brackets introduce arguments of functions, whereas square brackets specify the sequence of operations.

2 Model of material

2.1 Kinematics

The material description developed in the paper is based on a thermo-elasto-plastic model presented in paper [2]. The model is based on the decomposition of the deformation gradient into reversible part $\mathbf{F}^r$, related to elastic deformation and thermal expansion, and irreversible (plastic) part $\mathbf{F}^p$ in the following form

$$\mathbf{F} = \mathbf{F}^r \mathbf{F}^p \tag{2.1}$$

The deformation gradient is defined in the standard form as $\mathbf{F} = \partial \mathbf{x}(\mathbf{X}, t)/\partial \mathbf{X}$ with $J = \det(\mathbf{F}) > 0$, where $\mathbf{X}$ and $\mathbf{x}$ are vectors denoting the referential and the current placement of a particle in the Cartesian coordinate system, respectively. The variable t represents time. Based on the decomposition (2.1) the reversible left Cauchy Green tensor is defined

$$\mathbf{b}^r = \mathbf{F}^r(\mathbf{F}^r)^{\mathrm{T}}, \qquad J^{br} = \det(\mathbf{b}^r) \tag{2.2}$$

The velocity gradient and its symmetric part, called the deformation rate, are defined as usually

$$\mathbf{l} = \dot{\mathbf{F}}\mathbf{F}^{-1}, \qquad \mathbf{d} = \frac{1}{2}\left(\mathbf{l} + \mathbf{l}^{\mathrm{T}}\right) \tag{2.3}$$

The dot over a quantity denotes its rate. The plastic velocity gradient is defined as follows

$$\mathbf{L}^p = \dot{\mathbf{F}}^p \left[\mathbf{F}^p\right]^{-1} \tag{2.4}$$

and the plastic deformation rate

$$\mathbf{d}^p = \frac{1}{2}\left(\mathbf{l}^p + [\mathbf{l}^p]^{\mathrm{T}}\right), \qquad \mathbf{l}^p = \mathbf{F}^r\mathbf{L}^p\left[\mathbf{F}^r\right]^{-1} \tag{2.5}$$

The Helmholtz free energy is assumed as dependent on the reversible left Cauchy-Green deformation tensor $\mathbf{b}^r$, internal variable α related to hardening and absolute temperature T

$$\psi = \psi(\mathbf{b}^r, \alpha, T) \tag{2.6}$$

The specific form of the Helmholtz free energy will be given in the subsequent subsection.

2.2 Governing equations

The first governing equation, i.e. the balance of linear momentum for the large strain problem, is written for the quasi-static case with mass forces neglected [11]

$$\mathrm{div}(\boldsymbol{\tau}/J) = \mathbf{0} \tag{2.7}$$

where symbol $\mathrm{div}(\cdot)$ denotes the spatial divergence of quantity $\cdot$, and $\boldsymbol{\tau}$ is the Kirchhoff stress tensor. The quasi-static assumption results in neglecting the inertial term in Eq. (2.7). The model can then be applied to simulate deformation at low strain rates. Consequently, viscous effects are also neglected.

The second governing equation is the first law of thermodynamics, i.e. the balance of energy, which can be written using spatial quantities [2]

$$\rho\dot{u} = \boldsymbol{\tau} : \mathbf{d} - J\mathrm{div}(\mathbf{q}) \tag{2.8}$$

where ρ is the material density of the undeformed configuration which can be temperature dependent, u is the internal energy per unit of mass, and $\mathbf{q}$ is the Kirchhoff heat flux density vector. In Eq. (2.8) an external heat source (per unit of mass) is not taken into account.

The second law of thermodynamics, i.e. the dissipation inequality, can be written in the following form [2]

$$\rho T\dot{\eta} - \rho\dot{u} + \boldsymbol{\tau} : \mathbf{d} - \frac{J}{T}\mathbf{q} \cdot \mathrm{grad}(T) \geq 0 \tag{2.9}$$

In the above equation η denotes the entropy per unit of mass and $\mathrm{grad}(\cdot)$ is the spatial gradient of quantity $\cdot$. Using the Legendre transformation

$$\psi(\mathbf{b}^r, \alpha, T) = u(\mathbf{b}^r, \alpha, \eta - \eta T \tag{2.10}$$

after some manipulations the dissipation inequality can be written as

$$\left[\boldsymbol{\tau} - 2\rho\frac{\partial\psi}{\partial\mathbf{b}^r}\right] : \mathbf{d} + \left[2\rho\frac{\partial\psi}{\partial\mathbf{b}^r}\mathbf{b}^r\right] : \mathbf{d}^p - \rho\frac{\partial\psi}{\partial\alpha}\dot{\alpha} - \frac{J}{T}\mathbf{q}\cdot\mathrm{grad}(T) \geq 0 \tag{2.11}$$

Because inequality (2.11) should be fulfilled for any arbitrary $\mathbf{d}$, the Kirchhoff stress tensor is equal to

$$\boldsymbol{\tau} = -2\rho\frac{\partial\psi}{\partial\mathbf{b}^r} \tag{2.12}$$

The thermodynamic force conjugated to α is defined as

$$\beta = \rho\frac{\partial\psi}{\partial\alpha} \tag{2.13}$$

Now the reduced form of the dissipation inequality is obtained

$$\underbrace{[\boldsymbol{\tau}:\mathbf{d}^p - \beta\dot{\alpha}]}_{\mathcal{D}_{mech}} + \underbrace{\left[-\frac{J}{T}\mathbf{q}\cdot\mathrm{grad}(T)\right]}_{\mathcal{D}_{therm}} \geq 0 \tag{2.14}$$

Is is assumed that both parts of the dissipation, mechanical $\mathcal{D}_{mech}$ and thermal $\mathcal{D}_{therm}$, are greater than or equal to zero. In the former case, the inequality is fulfilled by the application of the isotropic spatial Fourier law as the constitutive relation for the heat flux density vector, for details see [12],

$$\mathbf{q} = -Jk\,\mathrm{grad}(T) \tag{2.15}$$

where k is the conductivity coefficient which can be temperature-dependent, i.e. $k(T)$.

Using Eqs. (2.10) and (2.11) the energy balance equation (2.8) can be rewritten in the so-called temperature form which will be further implemented in numerical simulations

$$c\dot{T} = J\mathrm{div}(\mathbf{q}) + \mathcal{D}_{mech} + \mathcal{H} + \mathcal{A} \tag{2.16}$$

where

$$c = -\rho T\frac{\partial^2\psi}{\partial T^2} \tag{2.17}$$

$$\mathcal{H} = \left[2\rho T\frac{\partial^2\psi}{\partial T\partial\mathbf{b}^r}\mathbf{b}^r\right] : [\mathbf{d} - \mathbf{d}^p] \tag{2.18}$$

$$\mathcal{A} = \rho T\frac{\partial^2\psi}{\partial T\partial\alpha}\dot{\alpha} \tag{2.19}$$

In Eq. (2.16) there are three internal (structural) sources of heating/cooling, which can change the temperature of the material even if there are no external heat sources. $\mathcal{D}_{mech}$ is related to the heat production during a plastic process and $\mathcal{H}$ to the thermo-elastic source of heating/cooling. The term $\mathcal{A}$ is in turn a source related to the coupling between hardening in plasticity and temperature, which will further be called temperature-hardening coupling. This term is active when the plastic part of the free energy function is temperature-dependent.

Note that the internal sources depend on the adopted form of the Helmholtz free energy which will be specified in the next subsection.

2.3 Helmholtz free energy

In this paper the following decoupled form of Helmholtz free energy is adopted

$$\psi = \psi^r(\mathbf{b}^r, T) + \psi^p(\alpha, T) + \psi^\theta(T) \tag{2.20}$$

where ψ^r is the free energy related to the reversible deformation due to elastic response and thermal expansion, ψ^p is the plastic part which can be dependent on the hardening variable and optionally on temperature. The reversible part of the free energy follows the Neo-Hookean formulation which is a basic approach for elastic materials in a large deformation framework. The last term ψ^θ is the purely thermal part. The specific form of reversible Helmholtz free energy is given below

$$\psi^r(\mathbf{b}^r, T) = \frac{1}{\rho(T)} \left[\frac{\kappa(T)}{2} \left[\ln\left(\sqrt{J^{br}}\right) \right]^2 + \frac{G(T)}{2} \left[\mathrm{tr}\left([J^{br}]^{-1/3} \mathbf{b}^r \right) - 3 \right] - 3\kappa\,\alpha_T(T)\,[T - T_0]\ln\left(\sqrt{J^{br}}\right) \right] \tag{2.21}$$

The temperature-dependence of the material parameters present in Eq. (2.21) is now explicitly written. The symbol κ denotes the bulk modulus, G – the shear modulus, and α_T – thermal expansion coefficient.

The plastic part of the free energy is related to exponential hardening which is observed for the considered aluminum alloy, cf. [6, 10]. The form of the plastic part of the free energy influences also the source defined in Eq. (2.19). In this case two models are compared.

The first one, called further *Model 1*, incorporates the plastic free energy function depending on the hardening variable and temperature. The temperature dependency is achieved by the application of temperature-dependent parameters: the initial and the final yield stresses σ_{y0} and $\sigma_{y\infty}$, respectively, as follows

$$\psi^p(\alpha, T) = \frac{1}{\rho} \left[\sigma_{y\infty}(T) - \sigma_{y0}(T) \right] \left[\alpha + \frac{1}{\delta} \exp(-\delta\alpha) \right] \tag{2.22}$$

The final yield stress represents the saturated flow stress, i.e. the maximum stress level the material can reach after a large amount of plastic deformation, when further hardening becomes negligible. The example of such assumption can be found e.g. in [5]. For Model 1 the temperature-hardening coupling is present and in the energy balance equation (2.16) the term $\mathcal{A}$ in non-zero. The saturation parameter δ in Eq. (2.22) is assumed in the paper as constant.

The second model, called further *Model 2*, includes temperature-independent plastic part of the free energy function

$$\psi^p(\alpha) = \frac{1}{\rho} \left[\sigma_{y\infty}(T_0) - \sigma_{y0}(T_0) \right] \left[\alpha + \frac{1}{\delta} \exp(-\delta\alpha) \right] \tag{2.23}$$

and involves the values of the initial and the final yield stresses at initial temperature of the experiment T_0. The temperature-independent plastic part of the free energy function is used e.g. in [4].

The thermal part of the free energy is not specified here explicitly. It is assumed that it has such a form that the heat capacity from Eq. (2.17) is temperature-dependent in a form given in the next section.

2.4 Plasticity

The yield function is assumed in the following form

$$\mathcal{F} = f(\boldsymbol{\tau}) - \sigma_y(\alpha, T) \le 0 \tag{2.24}$$

where $f(\boldsymbol{\tau})$ is a stress measure governing plasticity, here the Huber-Mises measure is applied

$$f(\boldsymbol{\tau}) = \sqrt{\mathbf{t} : \mathbf{t}}, \qquad \mathbf{t} = \boldsymbol{\tau} - \frac{1}{3}\mathrm{tr}(\boldsymbol{\tau})\mathbf{I} \tag{2.25}$$

The yield stress $\sigma_y(\alpha, T)$ for Model 1 is assumed in a form

$$\sigma_y(\alpha, T) = \sigma_{y0}(T) + \beta(\alpha, T) = \sigma_{y0}(T) + [\sigma_{y\infty}(T) - \sigma_{y0}(T)] [1 - \exp(-\delta\alpha)] \tag{2.26}$$

whereas for Model 2 it is as follows

$$\sigma_y(\alpha, T) = \sigma_{y0}(T) + s(T)\beta(\alpha) = \sigma_{y0}(T) + s(T) [\sigma_{y\infty}(T_0) - \sigma_{y0}(T_0)] [1 - \exp(-\delta\alpha)] \tag{2.27}$$

where the thermal softening function $s(T)$ is proposed in the following form to obtain the same yield stress as in Model 1

$$s(T) = \frac{\sigma_{y\infty}(T) - \sigma_{y0}(T)}{\sigma_{y\infty}(T_0) - \sigma_{y0}(T_0)} \tag{2.28}$$

The associative flow rule is adopted in the following form

$$-\frac{1}{2}\mathcal{L}_v(\mathbf{b}^r) = \dot{\gamma}\frac{\partial \mathcal{F}}{\partial \boldsymbol{\tau}}\mathbf{b}^r \tag{2.29}$$

where the Lie derivative of the reversible left Cauchy-Green deformation tensor is defined as [2]

$$\mathcal{L}_v(\mathbf{b}^r) = \mathbf{F}\frac{\partial}{\partial t}\left[\mathbf{F}^{-1}\mathbf{b}^r\mathbf{F}^{-T}\right]\mathbf{F}^{\mathrm{T}} \tag{2.30}$$

and $\dot{\gamma}$ is the plastic multiplier which is related with the hardening variable through the equation $\alpha = \sqrt{2/3}\dot{\gamma}$.

The standard Kuhn-Tucker conditions complete the plasticity description

$$\dot{\gamma} \geq 0, \qquad \mathcal{F} \leq 0, \qquad \dot{\gamma}\mathcal{F} = 0 \tag{2.31}$$

3 Temperature-dependent parameters

The temperature-dependent parameters of aluminum alloy AW5083 related to both the mechanical and the thermal properties are based on the literature, in particular on [6] and [7]. Paper [6] provides the values of the density, Young modulus, heat conductivity, heat capacity, initial yield stress and final yield stress at the selected temperatures in the range from room temperature up to 500°C, denoted with red dots in Figs 1-6. The temperature on the horizontal axes is given in Kelvins. The blue lines in the figures represent approximations obtained using the least square method for the assumed basis functions. In particular they are polynomial of a selected degree for the Young's modulus, density, heat conductivity and heat capacity, and logistic for the initial and final yield stresses.
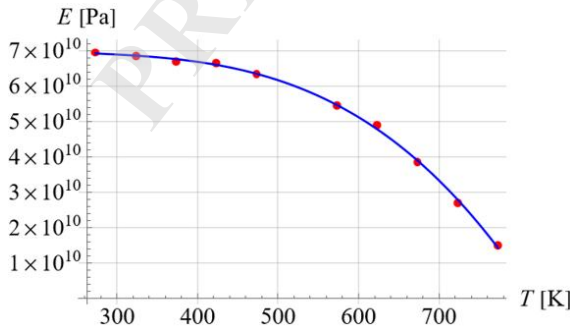

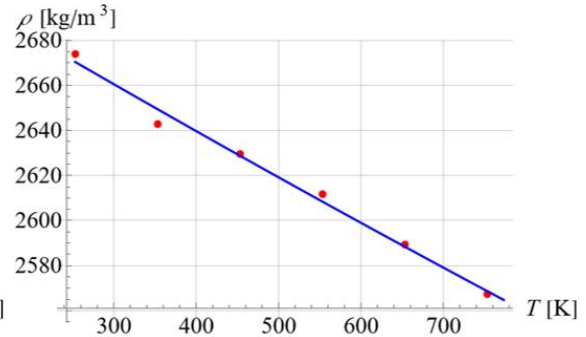Figure 1: Young's modulus vs. temperature.

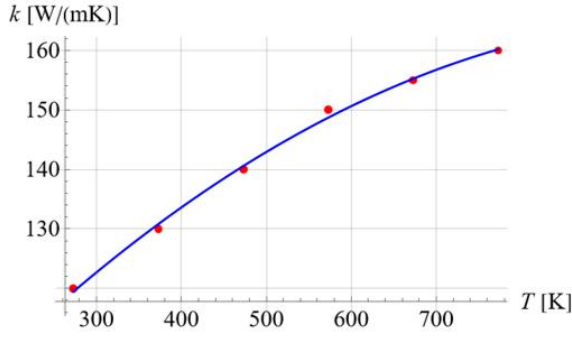Figure 2: Density vs. temperature.
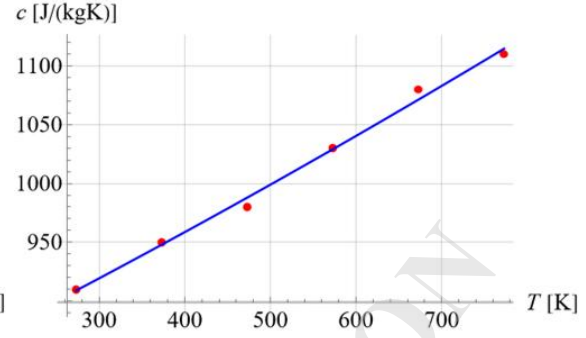
Figure 3: Heat conductivity vs. temperature.

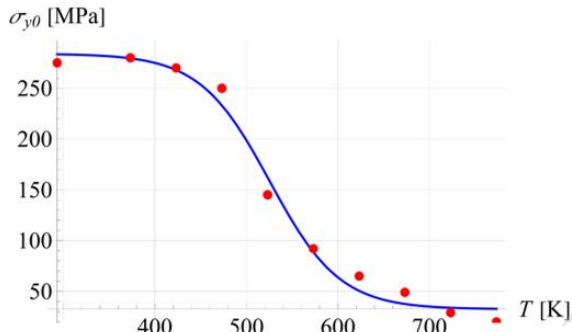Figure 4: Heat capacity vs. temperature.
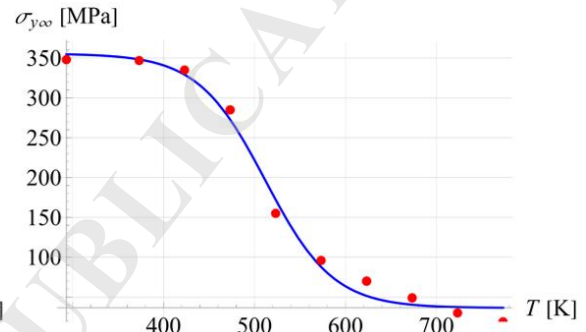

Figure 5: Initial yield stress vs. temperature.

Figure 6: Ultimate yield stress vs. temperature.

The diagram of the thermal expansion coefficient in Fig. 7 is prepared basing on the information provided in [7].
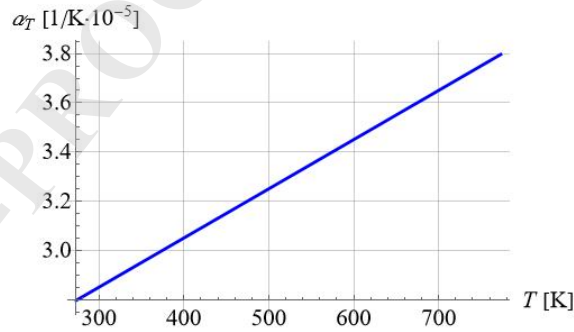

Figure 7: Thermal expansion coefficient vs. temperature.

The specific formulas describing the temperature-dependent parameters are given in Table 1. The proper values of the parameters are obtained for temperature given in Kelvins. In the last column the unit of the output is given.

7

Quantity	Formula	Unit
Density	$\rho(T) = 2724.97 - 0.219593\,T + 1.58929 \times 10^5\,T^2$	kg/m^3
Young's modulus	$E(T) = 7.7915 \times 10^{10} - 7.98531 \times 10^7\,T + 273938\,T^2 - 358.197\,T^3$	Pa
Thermal expansion coeff.	$\alpha_T(T) = 2.25 \times 10^{-5} + 2 \times 10^{-8}\,T$	1/K
Heat conductivity	$k(T) = 80.2766 + 0.165482\,T - 8.03571 \times 10^5\,T^2$	W/(mK)
Heat capacity	$c(T) = 807.914 + 0.355393\,T + 5.35714 \times 10^5\,T^2$	J/(kgK)
Initial yield stress	$\sigma_{y0}(T) = 2.83973 \times 10^8 - \dfrac{2.51535 \times 10^8}{1 + \exp(13.769 - 0.0262\,T)}$	Pa
Ultimate yield stress	$\sigma_{y\infty}(T) = 3.55575 \times 10^8 - \dfrac{3.19238 \times 10^8}{1 + \exp(13.827 - 0.027\,T)}$	Pa

Table 1: Material parameters depending on temperature.

It is assumed that the Poisson ratio is constant and equals $\nu = 0.3$. The bulk and shear moduli present in Eq. (2.21) are calculated on the basis of Young's modulus and Poisson's ratio in a standard way

$$G(T) = \frac{E(T)}{2[1+\nu]}, \qquad \kappa(T) = \frac{E(T)}{3[1-2\nu]} \tag{3.1}$$

The value of the saturation parameter is assumed to be equal to $\delta = 19.618$, see [10].

4 Numerical simulations

4.1 Implementation

The numerical verification of the presented models of the aluminum alloy with the temperature-dependent parameters is performed using the finite element method. The model is implemented within symbolic-numerical packages of *Wolfram Mathematica* called *AceGen/AceFEM*, see e.g. [9]. The finite element code is developed for three-dimensional hexahedral finite elements with the linear interpolation of temperature and displacement fields and so-called *F-bar* modification [13] preventing the volumetric locking which occurs for Huber-Mises plasticity. The implementation of large strain plasticity can be found in [9] whereas the implementation of the coupled thermomechanical model is presented in [14].

Numerical tests include two elongated specimens, in particular one cubic finite element in uniaxial tension state and a dogbone sample which is used commonly for experiments in laboratory, see [10]. For the former sample the elastic stage is analyzed firstly and next the plastic one occurring for a greater loading is investigated.

The attention is focused on the internal heat sources and their influence on the sample behavior at room temperature and at elevated temperatures up to 500°C (i.e. 773.15 K).

4.2 Uniaxial tension test

A simulation of one finite element (FE) in uniaxial tension is conducted. The cubic specimen has dimensions $L = 10$ mm, $W = 10$ mm, $H = 10$ mm. The visual representation of the finite element in three-dimensional (3D) space can be seen in Fig. 8. Mechanical boundary conditions are assumed in such a way that a uniform deformation is reproduced and free transverse deformation is allowed. Insulation is applied as thermal boundary conditions.
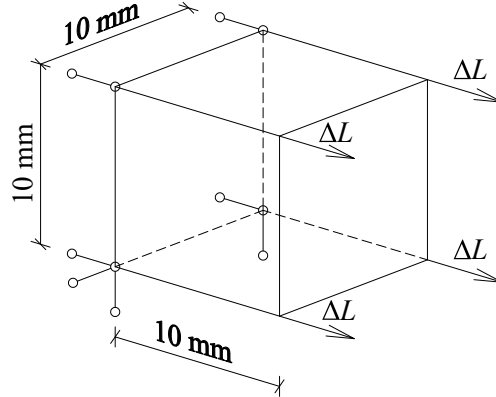
Figure 8: Visual representation of 1 FE in 3D

4.2.1 Elastic regime analysis

Firstly, the sample is subjected to enforced elongation equal to $\Delta L = L/180 = 0.056$ mm applied in time $t = 10$ s. Such elongation allows for the simulation of the sample in the elastic range of as well as the beginning of the plastic deformation phase.

In Fig. 9 reaction diagrams versus the enforced displacement for different initial temperatures T_0, i.e. 20, 100, 200, 300, 400 and 500°C, are presented. With the increase of the initial temperature, the stiffness of the sample decreases. This phenomenon manifests itself on the graph as a decreasing tendency of the gradient. It is shown that the material subjected to elongation enters the plastic range of deformation at different values of ΔL depending on the initial temperature of the sample T_0, which is an effect of dependence of the initial yield stress on temperature. When the temperature rises, the yield stress decreases. Through the numerical analysis, it is found that the elastic deformation range is the shortest at initial temperature $T_0 = 400$°C. Although the initial yield stress is lower at temperature 500°C, the elastic stiffness is significantly smaller and this causes the onset of plasticity to occur later.
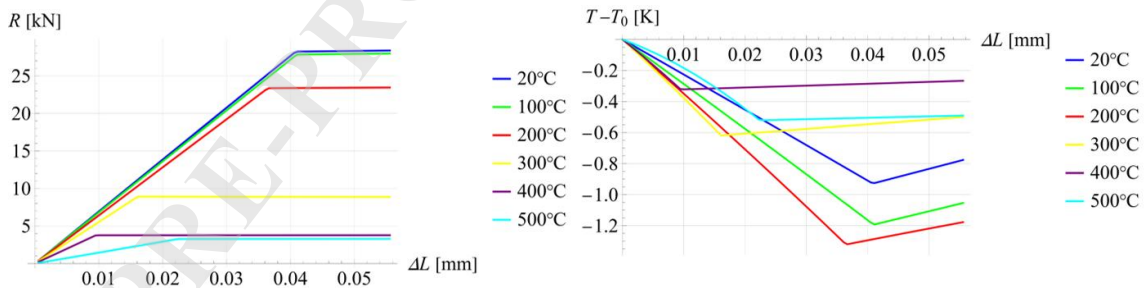
Figure 9: Sum of reactions vs enforced displacement for different initial temperatures

Figure 10: Relative temperature of the sample vs enforced displacement for different initial temperatures

In Fig. 10 a change in the temperature of the sample is shown versus to applied elongation, for the analyzed initial temperatures. In the elastic range of deformations a decrease in the temperature of the sample is seen, and the Gough-Joules effect is observed, which manifests itself as thermo-elastic cooling. An upward tendency of the curves starts at a point at which the behavior of the sample changes, and the material enters the plastic range of deformations. The results of the test presented in Fig. 10 show that

9

depending on the initial temperature the sample enters the state of irreversible deformations at different stages of elongation. It is noted that the biggest thermo-elastic cooling effect is observed for the initial temperature $T_0 = 200°C$.

To investigate the influence of the thermo-elastic cooling on the material behavior more thoroughly Fig. 11 is prepared. It presents the relative temperature at the stage of deformation $\Delta L = 0.0095$ mm for the analyzed initial temperatures. This loading step is the last one at which all tested samples undergo elastic deformation. It can be observed that the strongest effect of the thermo-elastic cooling at the analyzed stage of deformation is for the initial temperature $T_0 = 300°C$. As the initial temperature grows from $T_0 = 20°C$ up to $T_0 = 300°C$ the absolute value of relative temperature increases gradually. After reaching the $300°C$ threshold, the absolute value of relative temperature starts to decrease. This a result of the value of thermo-elastic cooling source presented in Fig. 12. The observed phenomenon can be explained as follows. In the analyzed model, the thermo-elastic cooling depends on temperature in two ways, see Eq (2.18). Firstly, along with the rising absolute temperature of the sample the value of the cooling source due to thermo-elastic coupling increases. Secondly, the cooling source is also dependent on the elastic parameters of the material, especially on the Young modulus which decreases with the temperature increase, see Fig. 1. At temperature 623.15 K = 350°C the Young modulus is reduced almost by half. From this moment on, the second effect dominates, which is the decrease of the source of cooling because of the decreasing stiffness of the material.
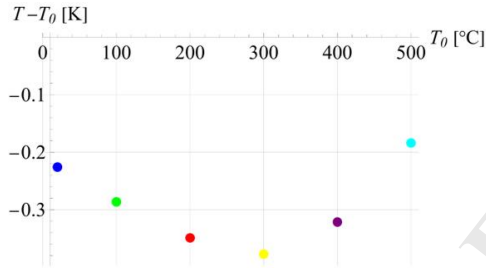

Figure 11: Relative temperature at $\Delta L = 0.0095$ mm for tests conducted for different initial temperatures
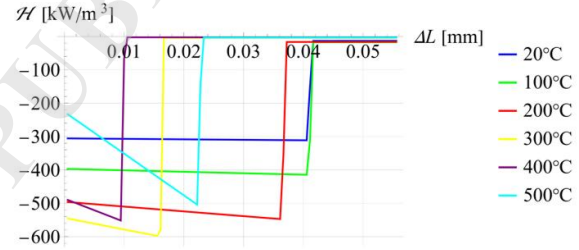
Figure 12: Elastic cooling for tests conducted for different initial temperatures

4.2.2 Plastic regime analysis

The cubic sample is now subjected to enforced elongation $\Delta L = L/5 = 2$ mm applied in time 1 s, resulting in the plastic deformation. Fig. 13 and Fig. 14 depict the relationship between the sum of reactions and the enforced displacement for the sample shown in Fig. 8. Both diagrams present the influence of the initial temperature on the mechanical response of the material, but they differ in the type of the constitutive model used for testing of the samples. The results obtained for Model 1 are presented in Fig. 13 and for Model 2 in Fig. 14. The graphs capture the transition from elastic to plastic deformation, where the sum of reactions exhibits nonlinear behavior as the displacement increases. Higher initial temperatures typically reduce the yield stress and hardening modulus of aluminum due to thermal softening. This can manifest itself as lower reaction forces for equal displacements in Fig. 13 and Fig. 14 for elevated temperatures. Comparing the reactions for Model 1 and Model 2 one can see that a visible difference is present only for two examined reference temperatures: $T_0 = 200°C$ and $T_0 = 250°C$. In comparison with Model 1, Model 2 shows stronger softening of the material at initial temperature 200°C. A larger softening can also be observed for the temperature $T_0 = 250°C$. After closer examination of the obtained results the differences in reactions at the end of the process between the two models is equal to 8.2% for the initial temperature 200°C, and 17.1‰
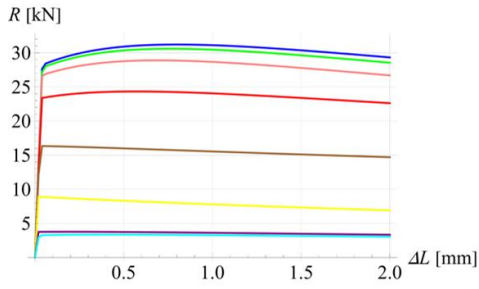
for the initial temperature 500°C.

Figure 13: Sum of reactions vs enforced displacement for different initial temperatures for Model 1
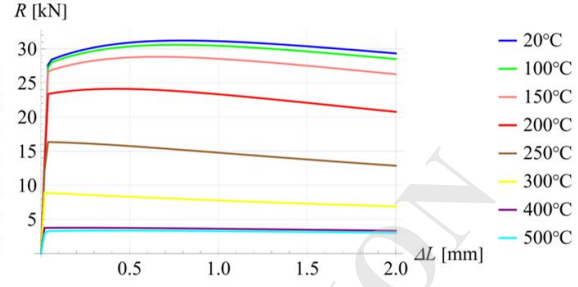

Figure 14: Sum of reactions vs enforced displacement for different initial temperatures for Model 2

Fig. 15 and Fig. 16 illustrate the evolution of relative temperature in the aluminum sample subjected to progressive elongation, culminating in plastic deformation. The graphs emphasize the thermomechanical coupling inherent to plastic work and dissipation, with distinct curves representing different initial temperatures. For the elastic regime the relative temperature drop is observed as expected. For the plastic phase of deformation a pronounced increase in relative temperature occurs due to plastic work conversion to heat. The slope of the diagram of relative temperature vs displacement grows post-yield, reflecting greater energy dissipation. For higher initial temperatures T_0 the sample exhibits lower values of $T - T_0$ at similar displacements due to lower dissipation. Model 2 reproduces higher heating of the sample comparing with Model 1.
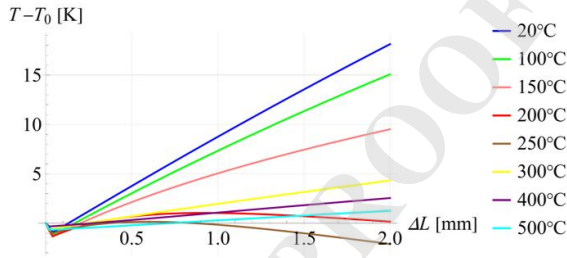
Figure 15: Relative temperature in the sample vs enforced displacement for different initial temperatures with Model 1
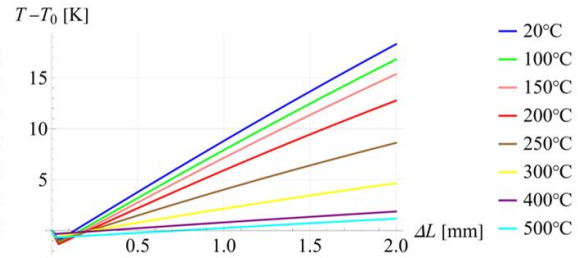

Figure 16: Relative temperature in the sample vs enforced displacement for different initial temperatures with Model 2

Figs. 17 and 18 present relative temperature $T - T_0$ measured in the aluminum sample at the end of the process, i.e. for the enforced displacement of 2 mm for varying initial temperatures. The graphs compare how temperature evolution differs for various thermomechanical starting conditions. It is clear that the response of the material differs depending on the type of the computational model applied.

For initial temperature $T_0 = 20°$ the difference is hardly noticeable, but for elevated temperatures the sample tested with Model 1 exhibits smaller raise in relative temperature, than samples tested with Model 2. The biggest difference in temperature at the end of the process is observed for $T_0 = 200°C$. For Model 1 the difference is 0.167 K, which means the temperature is almost the same as the reference temperature. For Model 2 it is 20.766 K, which makes for a 20.6 K difference between the applied models. The analysis presented in Section 4.2.1 shows, that for $T_0 = 200°C$ the elastic cooling effect is strong. The heat source

associated with plasticity is balanced by the relatively strong Gough-Joule effect, but not exclusively. In Model 1 the heat sources arising from plasticity include not only dissipation, but also the source due to the dependence of material parameters on temperature in the plastic part of the Helmholtz free energy. In such case this effect manifests itself as heat sinking, which additionally reduces the influence of dissipation. When assuming ψ^p as in Model 2, which is independent of temperature, the sinking effect is omitted, which allows for stronger heating of the sample. It is also important that in Model 1 the reduced heating causes smaller thermal softening, which explains why in Fig. 13 the reactions for $T_0 = 200°$C are much larger for Model 1 than for Model 2. Comparing the graphs from Figs. 17 and 18, one can notice that Model 2 provides a regular distribution of the results over the entire range of analyzed temperatures, therefore an approximation carried out for the given points decreases monotonously. In turn for Model 1, with the increase of the initial temperature, the temperature at the end of the process decreases to the point marked in brown, then rises for temperature $T_0 = 300°$C. Further on, a downward trend line is observed again.
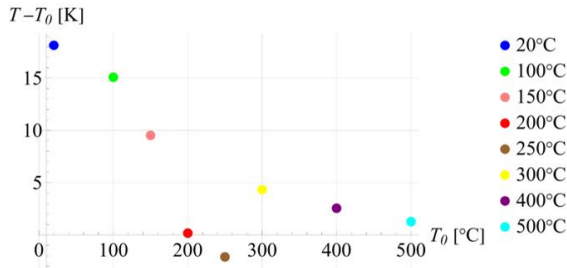

Figure 17: Relative temperature at $\Delta L = 2$ mm for tests conducted with different initial temperatures with Model 1
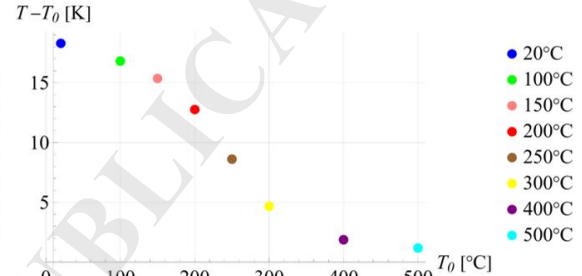

Figure 18: Relative temperature at $\Delta L = 2$ mm for tests conducted with different initial temperatures with Model 2

The quantitative analysis of heating (or sinking) sources for Model 1 can be performed on the basis of Figs. 19 and 20. The dissipated energy decreases with increasing initial temperature. In contrast, the temperature-hardening coupling causes heat sinking which increases significantly with the growth of the initial temperature up to 200°C and then becomes smaller, and even exhibits heating for temperature 400°C. Note that for $T_0 = 200°$C in the middle of the process the plastic heating due to energy dissipation is counteracted by the heat sinking, cf. red diagrams for $\Delta L = 1$ mm in Fig. 19 and 20.
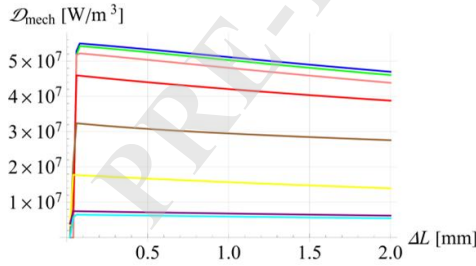

Figure 19: Dissipated mechanical energy for tests conducted for different initial temperatures with Model 1
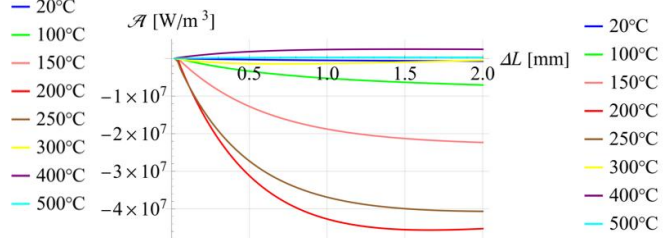

Figure 20: Heat source related to temperature-hardening coupling for Model 1

4.3 Dogbone specimen in tension

To reproduce real experimental testing conditions simulations are performed for a dogbone-shaped sample geometry described in work [10]. The geometry and dimensions of the sample are shown in Fig. 21. The thickness of the specimen is 2 mm. The sample is subjected to maximum elongation of $\Delta L = 30$ mm in time duration of $t_{max} = 4.95$ s.
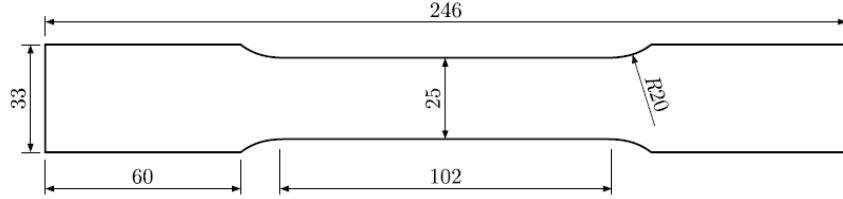

Figure 21: Dogbone-shaped sample – geometry and dimensions (in mm).

4.3.1 Tests for different meshes

The first set of simulations with Model 1 are performed for three different discretizations. In Fig. 22 one can find visual representation of the three meshes used for the tests. The first mesh includes 408 finite elements, the second 3 264, and the third 26 112 elements. In the thickness direction the coarsest mesh contains 1 finite element, medium mesh 2 finite elements, and the finest mesh has 4 finite elements. For mesh density analysis, the insulation boundary conditions on all surfaces are assumed and the initial temperature of the sample is the room temperature, i.e. $T_0 = 293.15$ K.

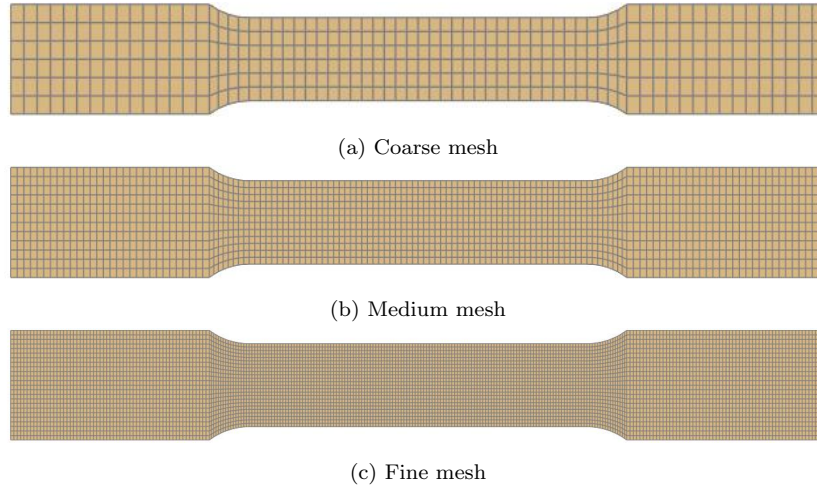(a) Coarse mesh

(b) Medium mesh

(c) Fine mesh

Figure 22: Visual representation of analyzed meshes

The reaction diagram obtained for the analyzed discretizations is presented in Fig. 23. For the thermo-elastic range the results for all three meshes coincide. The same conclusion can be made for the plastic range when material hardens, which takes place until about $\Delta L = 10$ mm. After the peak point the decreasing reaction diagrams for different meshes slightly diverge. The descending diagrams are a result of strain localization due to geometrical and thermal softening. Although the results do not coincide, the mesh dependence does not seem to be pathological: the results for the medium and the fine meshes are very close to each other. It is worth mentioning that heat conductivity present in the simulations has a regularizing
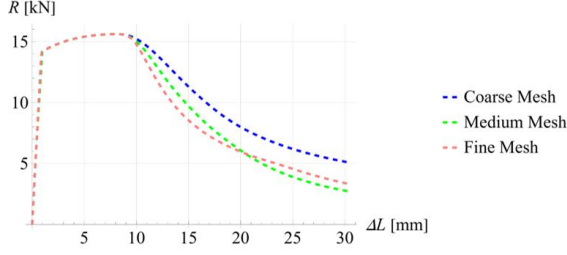
effect, cf. [15].

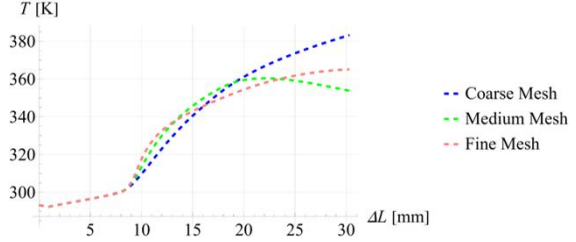Figure 23: Reactions depending on the mesh refinement in mid point of the sample

Figure 24: Temperature depending on the refinement of the mesh in mid point of the sample

It is observed in Fig. 24 that the temperature in the elastic range and in the hardening phase of plasticity is also the same for all meshes. When the localization of deformations occurs, the temperature starts increasing rapidly, because the temperature of the sample is read at the center of the specimen, where plastic deformations are the largest. It can also be noticed that the temperature for medium and fine mesh starts to decrease at a certain point, but it is not true for the coarsest mesh. Such phenomenon is an effect of different forms of localization observed in the considered meshes, which are presented in Fig. 25. For the coarse and medium meshes necking is visible, while for the fine mesh shear bands are present. The finest mesh is chosen for the remaining tests to preserve the accuracy of the obtained results.
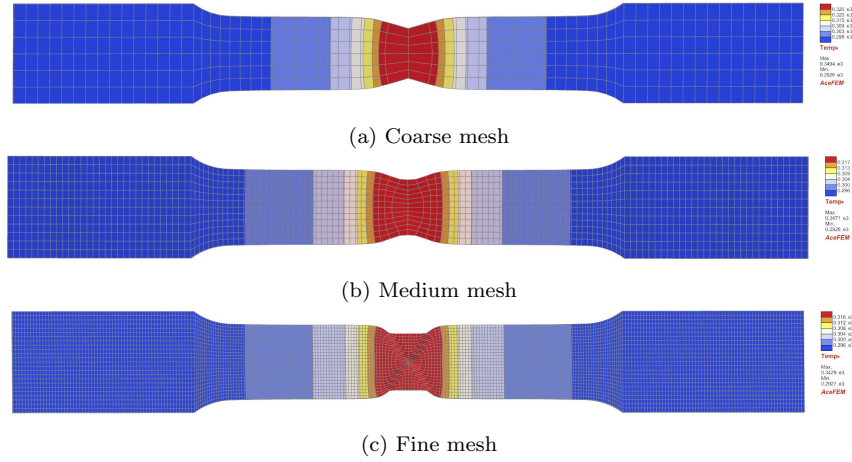

(a) Coarse mesh

(b) Medium mesh

(c) Fine mesh

Figure 25: Deformed meshes with temperature for $\Delta L = 30$ mm

4.3.2 Influence of thermal boundary conditions

The second set of simulations is performed for Model 1, room temperature and different thermal boundary conditions, i.e. for insulation and for convection. The heat flux density normal to the specimen surface with convection is defined in a following way

$$q_n = h_{conv}(T - T_\infty) \tag{4.1}$$

where T_∞ is the temperature of surrounding and h_{conv} is the convection coefficient. The parameters used in simulations are given in Table 2. The value $h_{conv} = 0$ means the insulation boundary condition.

14

Property	Symbol	Value	Unit
Temperature of surrounding	T_∞	T_0	K
Convection coefficient	h_{conv}	0, 10, 100	$J/(sKm^2)$

Table 2: Convection parameters.

The results shown in Fig. 22 for all convection coefficients h_{conv} taken into consideration, in the range of reversible deformations and in the plastic hardening range coincide. Starting from $\Delta L = 20$ mm the temperature stops increasing, and the sloping curves become increasingly different from each other. Such a phenomenon happens because of the presence of temperature-hardening coupling in Model 1. With a bigger convection coefficient, greater temperature decrease is observed. Fig. 26 shows that the reactions are independent of the chosen convection parameter. For the remaining tests convection coefficient $h_{conv} = 10$ is chosen. For tests performed at elevated temperatures is is assumed that $T_\infty = T_0$.
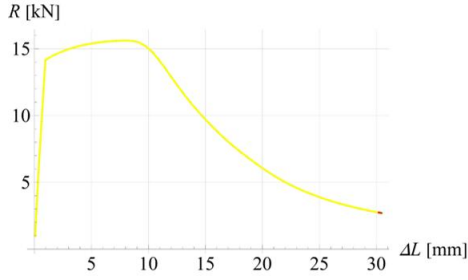

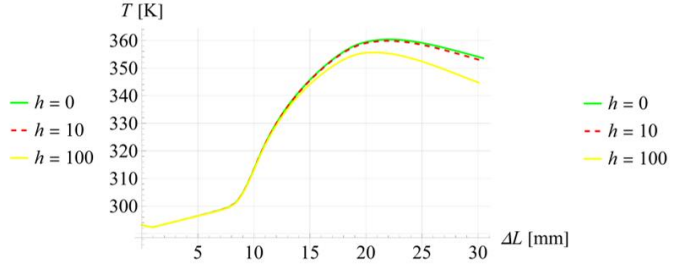Figure 26: Reactions independent of the convection coefficient

Figure 27: Temperature difference depending on the value of convection coefficient h_{conv}

4.3.3 Model 1 vs Model 2

The third and core set of simulations includes the tests of sample tension for different initial temperatures. Now the sample is subjected to elongation of $\Delta L = L/8 = 30.8$ mm in time duration of $t = 10$ s.

Figs. 28 and 29 show the reaction force versus the enforced displacement for Model 1 and Model 2, respectively. For higher initial temperatures, the magnitude of reactions decreases, which is consistent with the analysis performed for 1 FE. The biggest difference between the models is observed for temperature $T_0 = 200°C$, similarly to Fig. 14. For Model 2 the material softens earlier than for Model 1. Such behavior is a result of more substantial self-heating for Model 2, causing bigger thermal softening.
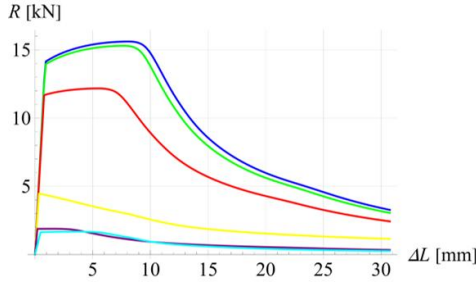
Figure 28: Sum of reactions vs enforced displacement for different initial temperatures for Model 1
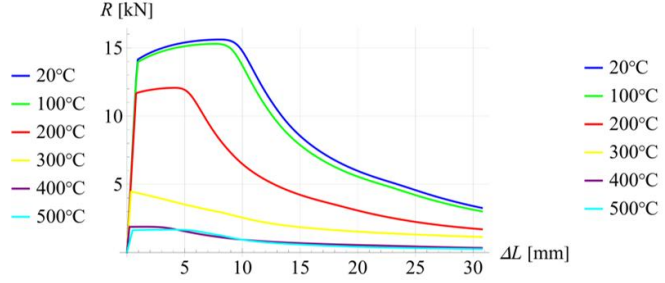

Figure 29: Sum of reactions vs enforced displacement for different initial temperatures for Model 2

Figs. 30 and 31 provide the comparison of temperature change versus elongation. Differences between the models are seen for all analyzed temperatures. Model 2 reproduces bigger temperature rise for lower T_0, but smaller rise for higher initial temperatures, i.e. $T_0 = 400°$C and $T_0 = 500°$C. A significant difference is observed for $T_0 = 200°$C as in this case the amount of source sinking due to temperature-hardening coupling exceeds the heat production due to plastic dissipation in the central part of the specimen where the localization zone occurs. It should also be explained that the results obtained for $T_0 = 300°$C are not comparative with the remaining results because in this case the localization zone is not at the center of the dogbone specimen where the temperature is read, see Fig. 32c. Due to that reason the temperature diagram shows a decrease in relative temperature as a result of unloading.

Figs. 32-35 present deformed meshes with temperature and hardening variable distributions for selected initial temperatures, i.e. 20°C, 200°C, 300°C. For $T_0 = 20°$C and $T_0 = 200°$C strain localization occurs in the middle part of the sample in the form of two shear bands. As it was mentioned above, the localization for T_0=300°C appears in two zones in the web. Only for Model 1 and $T_0 = 200°$C the highest temperature is not in the shear band areas but outside them. The reason is that thermo-plastic sinking in this case is so strong that the area of the active plastic process undergoes cooling. Comparing the temperature and hardening variable distributions, it can be observed that the temperature field is more diffused due to heat conductivity.
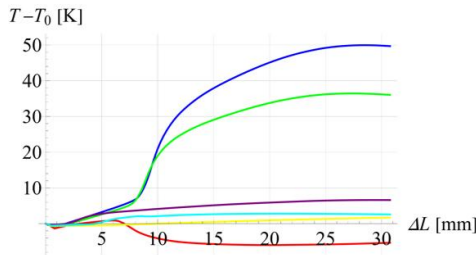

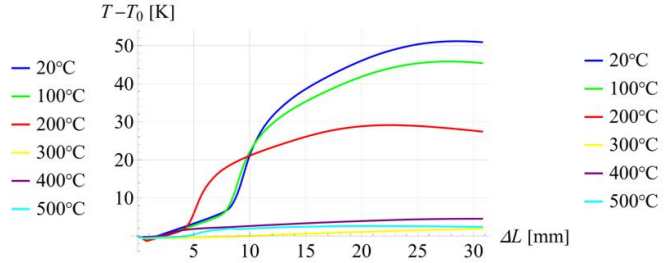Figure 30: Relative temperature vs enforced displacement for different initial temperatures for Model 1

Figure 31: Relative temperature vs enforced displacement for different initial temperatures for Model 2
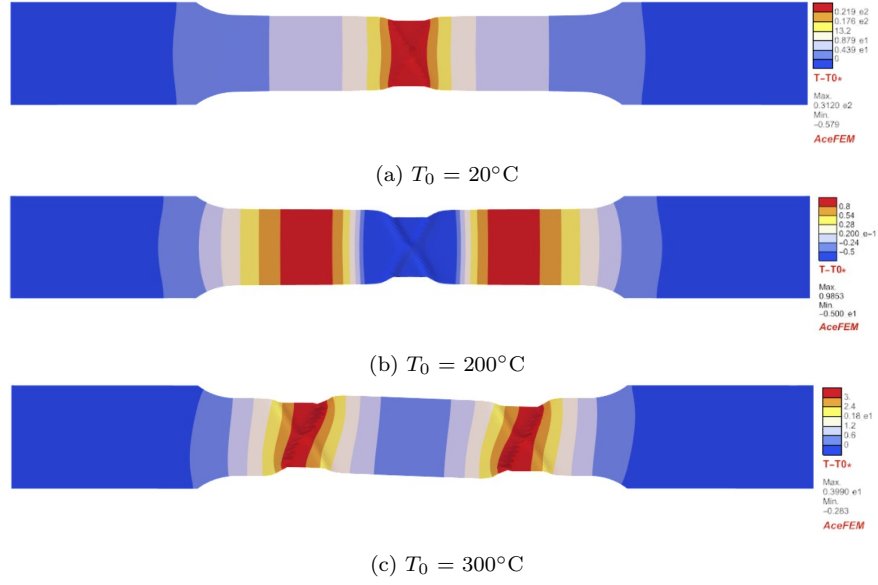
16

(a) $T_0 = 20°$C

(b) $T_0 = 200°$C

(c) $T_0 = 300°$C

Figure 32: Deformed mesh with relative temperature at $\Delta L = 12.3$ mm for Model 1

(a) $T_0 = 20°$C

(b) $T_0 = 200°$C

(c) $T_0 = 300°$C
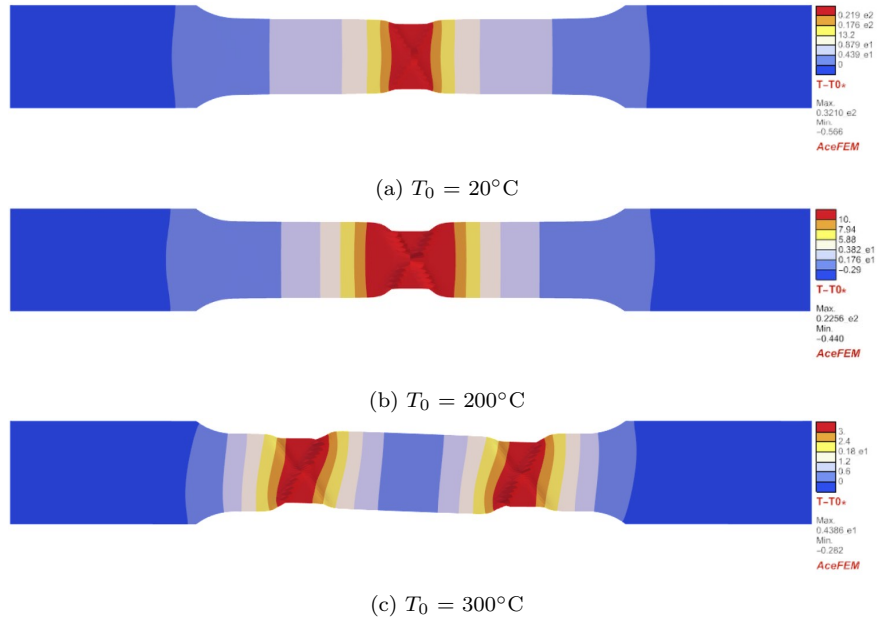
Figure 33: Deformed mesh with relative temperature at $\Delta L = 12.3$ mm for Model 2

(a) $T_0 = 20°$C

(b) $T_0 = 200°$C

(c) $T_0 = 300°$C
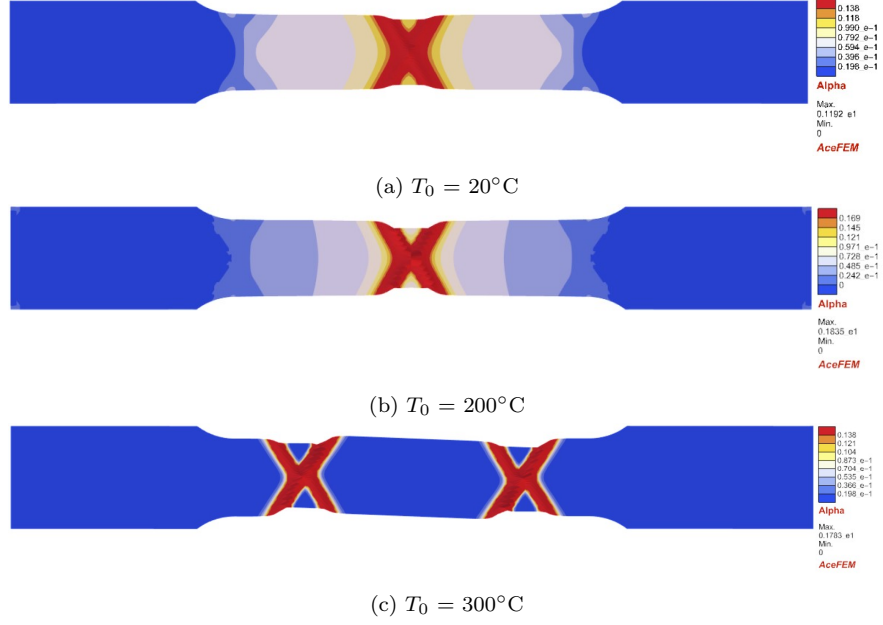
Figure 34: Deformed mesh with hardening variable at $\Delta L = 12.3$ mm for Model 1

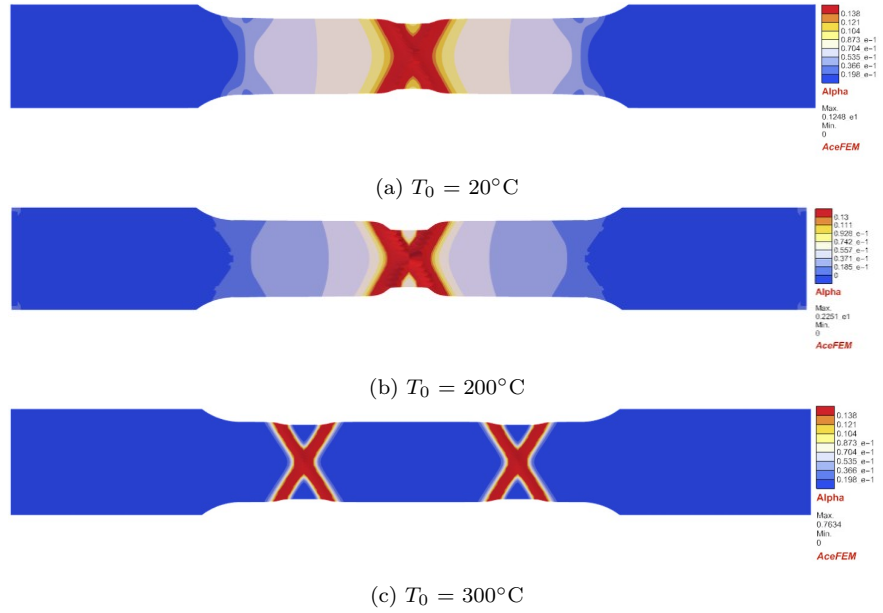(a) $T_0 = 20°$C

(b) $T_0 = 200°$C

(c) $T_0 = 300°$C

Figure 35: Deformed mesh with hardening variable at $\Delta L = 12.3$ mm for Model 2

5 Conclusions

The research presents a comprehensive numerical investigation of aluminum alloy AW5083 under tension loading, using large strain thermo-elasto-plastic models. An important aspect of the constitutive description is the application of temperature-dependent material parameters valid in the range from room temperature up to 500°C and the employment of internal heat sources. This allows for numerical simulations of the experiments performed at elevated temperatures. The study of plastic range of deformation is focused on

two models of the plastic part of the free energy function. The verification of the influence of temperature-dependent properties on the outcome is performed through simulations of 1 cubic FE and dogbone specimens. The models successfully capture fundamental thermo-mechanical phenomena, such as thermo-elastic cooling during elastic deformation and heat generation due to plastic dissipation.

The simulations at different initial temperatures reveal that the Gough-Joule effect is the strongest at initial temperature of $300°C$. The elastic modulus, yield stress and hardening parameters exhibit strong temperature dependence, leading to reduction of stiffness and earlier yielding at elevated initial temperatures (e.g. 400-$500°C$).

Mesh sensitivity studies show that a fine discretization is necessary to reproduce properly the localized deformation mode in the form of shear band(s). Coarser meshes underestimate post-peak softening and misrepresent the localization pattern limiting it to necking. The convection boundary conditions affect the temperature field. The higher convection coefficient causes accelerating of sample cooling and reduces thermal softening.

A thorough comparison between models including temperature-dependent and temperature-independent plastic free energy reveal that the largest discrepancies between the models occur at initial temperatures 200-$300°C$, where Model 2 predicts stronger material softening due to higher temperature increase. Model 1, including the additional source sinking term resulting from the temperature-hardening coupling, reduces the effect of plastic heating. Moreover, heat sinking for Model 1 is particularly significant in the temperature range of 100-$300°C$ and the observed disturbance in this range does not seem consistent with the physics.

Future work should focus on experimental validation in controlled thermal environments to calibrate and refine the models. This would provide crucial data for parameter identification and enhance the models' predictive capabilities. Additionally, extending the framework to include viscous effects, anisotropic behavior, and propagative instabilities such as Portevin-Le Chatelier bands would significantly broaden the model's applicability. Such developments would not only improve accuracy of the simulations but also contribute to safer and more efficient design of components exposed to extreme thermal and mechanical loads.

Acknowledgement

References

[1] Simo J.C., Numerical analysis and simulation of plasticity, [in:] Ciarlet P.G., Lions J.L. [ed.], *Handbook of Numerical Analysis, volume IV*, pp. 183–499, Elsevier Science B.V., Boca Raton, 1998.

[2] Ristinmaa M., Wallin M., Ottosen N. S., Thermodynamic format and heat generation of isotropic hardening plasticity. *Acta Mechanica*, **194**: 103–121, 2007, https://doi.org/10.1007/s00707-007-0448-6.

[3] Holzapfel G.A., *Nonlinear Solid Mechanics. A Continuum Approach for Engineering*, John Wiley & Sons, Chichester, 2000, https://doi.org/10.1023/A:1020843529530.

[4] Oppermann P., Denzer R., Menzel A., A thermo-viscoplasticity model for metals over wide temperature ranges - application to case hardening steel, *Computational Mechanics*, **69**: 541–563, 2022, https://doi.org/10.1007/s00466-021-02103-4.

[5] Ĉanadija M.,Brnić J., Associative coupled thermoplasticity at finite strain with temperature-dependent material parameters, *International Journal of Plasticity*, **20**: 1851–1874, 2004, https://doi.org/10.1016/j.ijplas.2003.11.016.

[6] Summers P.T., Chen Y., Rippe C.M., Allen B., Mouritz A.P., Case S.W., Lattimer B.Y., Overview of aluminum alloy mechanical properties during and after fires, *Fire Science Reviews*, **4**: 3, 2015, https://doi.org/10.1186/s40038-015-0007-5.

[7] European Committee for Standardization (CEN), *EN 1991-1-2:2002: Actions on structures - part 1-2: General actions - actions on structures exposed to fire*, Section 3.3. 2002.

[8] Wcisło B., Mucha M., Pamin J., Internal heat sources in large strain thermo-elasto-plasticity - theory and finite element simulations. *Journal of Theoretical and Applied Mechanics*, **62**: 293–306, 2024, https://doi.org/10.15632/jtam-pl/185614.

[9] Korelc J., Wriggers P., *Automation of Finite Element Methods*, Springer International Publishing Switzerland, 2016, https://doi.org/10.1007/978-3-319-39005-5.

[10] Mucha M., Rose L., Wcisło B., Menzel A., Pamin J., Experiments and numerical simulations of Lueders bands and Portevin-Le Chatelier effect in aluminium alloy AW5083, *Archives of Mechanics*, **75**(3): 301–336, 2023, https://doi.org/10.24423/aom.4204.

[11] Miehe C., Entropic thermoelasticity at finite strains. aspects of the formulation and numerical implementation, *Computer Methods in Applied Mechanics and Engineering*, **120**: 243–269, 1995, https://doi.org/10.1016/0045-7825(94)00057-T.

[12] Wcisło B., Pamin J., Rose L., Menzel A., On spatial vs. referential isotropic Fourier's law in finite deformation thermomechanics, *Engineering Transactions*, **71**(1): 111–140, 2023, https://doi.org/10.24423/EngTrans.2460.20230214.

[13] de Souza Neto E.A., Peric D., Owen D.R.J., *Computational methods for plasticity. Theory and applications*, John Wiley & Sons, Chichester, 2008, https://doi.org/10.1002/9780470694626.

[14] Wcisło B., Pamin J., Local and non-local thermomechanical modeling of elastic-plastic materials undergoing large strains, *International Journal for Numerical Methods in Engineering*, **109**(1): 102–124, 2017, https://doi.org/10.1002/nme.5280.

[15] LeMonds J., Needleman A., Finite element analyses of shear localization in rate and temperature dependent solids, *Mechanics of Materials*, **5**: 339–361, 1986, https://doi.org/10.1016/0167-6636(86)90039-6.